

Electrochemical Corrosion of Sintered Composites on the basis of Fe/FePO₄ Coated Powders

Eva Dudrová^{1,*}, Margita Kabátová¹, Renáta Oriňáková², Pavol Hvizdoš¹

¹ Institute of Materials Research of SAS, Watsonova 47, 040 01 Košice, Slovakia

² Dpt. of Physical Chemistry, Faculty of Science, P.J. Šafárik University, Moyzesova 11, 041 54 Košice, Slovakia

*E-mail: edudrova@imr.saske.sk

Received: 28 September 2015 / Accepted: 17 November 2015 / Published: 1 January 2016

Electrochemical corrosion behaviour of sintered composites based on iron powder consisting of spherically and/or irregularly shaped iron particles precipitation coated with FePO₄ layer was studied using the potentiodynamic polarization test. The Fe/FePO₄ coated powders containing 2 and 5 wt-% of FePO₄ were compacted to the density of 6650-6700 kg m⁻³ and subsequently sintered at temperatures ranging from 912 to 1130°C for 3 min in air. The creation of a liquid phase during heating to 1130°C with subsequent quenching into water and/or into liquid nitrogen resulted in the formation of a thin and continuous iron phosphate layer consisting of ~ 85 wt-% of fine lamellar phase identified as graffonite and ~ 15 wt-% of iron oxides - wüstite, magnetite and hematite. Thus prepared composites show an improvement in anti-corrosion behavior, which is associated with the formation of a protective continuous layer. Silica nano-powder particles tend to agglomerate, which results in discontinuities in the protective iron phosphate layer, with a detrimental effect on corrosion behavior of these composites.

Keywords: Sintered composites iron/iron phosphate, electrochemical corrosion, corrosion behaviour, microstructure.

1. INTRODUCTION

Generally, inorganic phosphate compounds are regarded as corrosion inhibitors for iron and carbon steel in near neutral pH of the solutions [1, 2, 3]. Phosphate species are commonly used in paints to increase corrosion resistance of iron and steel, e.g. [4]. Iron phosphate FePO₄ intensively reacts with iron ions from the substrate to form compounds that precipitate at the interface. Rebeyrat et al. [5] have shown that the formation of a phosphate layer on the surface of iron powder particles

induces a significant improvement of the oxidation resistance in the temperature range 300–700°C. The phosphate layer is porous and does not provide effective protection against surface corrosion; and often this forms the preparation for further anti-corrosion treatment [6]. Volkland et al. [7] have described the Vivianite $[\text{Fe}_3(\text{PO})_4 \cdot 8\text{H}_2\text{O}]$ layer created by the action of bacterial activity which provides a significant corrosion inhibitor for mild steel. Crystalline ferrous phosphate species are referred as potential candidates for application in optical and electro-chemical areas [8–11], as well as for catalysis and ionic exchange [8]. The FePO_4 compound is also used in the steel and glass industries [12] and Fe_3PO_7 was considered as a potential electrode material [11].

The phosphate glasses, in the last few years, are the subject of considerable interest in both technological and scientific fields, especially due to the possibility to produce new glass composites with high chemical and thermodynamic stability [13, 14]. Various phosphate glasses can be used, among other applications, in the hermetic sealing of metallic and ceramic materials and optical applications [15], as well as for a nuclear waste immobilization, e.g. [16]. As was reported by Brow [17], phosphate glasses have been developed for a variety of specialty applications. Amorphous lithium phosphate [18] and phosphorus oxynitride glasses [19], for example, have fast ion conductivity which makes them useful as solid state electrolytes. However, most of phosphate glasses have relatively poor chemical durability. Ray et al. [20] have reported that the introduction of Fe_2O_3 results in the formation P-O-Fe bonds, and leads to improvement in the chemical durability of this modified phosphate glass. Iron phosphate glasses have generally excellent chemical durability and low melting temperature, typically between 950 and 1100°C [21]. Iron as a glass component significantly increases chemical durability, while the 60 P_2O_5 –40 Fe_2O_3 (Fe/P = 0.67) glass has the highest chemical durability. Donald et al. [22] and Ojovan [23] indicated that iron strengthens the chemical bonds in the iron phosphate glass structure, making their properties comparable or even better than those of borosilicate glasses. Iron phosphate glasses have the melting temperature of about 100–200 K lower than borosilicate glass and also, due to lower viscosity of the melts, their homogenization time is about 1.5–3 hours shorter [24]. Currently, iron phosphate glasses are considered also to be suitable for vitrification of waste, e.g. [17, 23, 25].

As powder metallurgy is the technology of processing powdered materials into net-shaped structural parts, it is also appropriate for the production of sintered composites on the basis of coated powders, whereby the components with special functional properties for required applications can be obtained. In our previous paper [26] thermally dependent microstructural and phase changes in the iron phosphate layer, resulting from sintering of composites prepared from the Fe/ FePO_4 coated powder with spherically shaped particles, were studied. The results reported in our paper [26] can be briefly summarized as follows: The ferric phosphate layer calcined in air at 400°C comprises three regions - the first, located at the Fe-substrate, contains iron oxides, an inter-region is formed of FePO_4 , the third region is composed of Fe_3O_4 and $\gamma\text{-Fe}_2\text{O}_3$ iron oxides, while $\gamma\text{-Fe}_2\text{O}_3$ transformed to $\alpha\text{-Fe}_2\text{O}_3$ iron oxides. X-ray powder diffraction confirmed the presence Fe_3O_4 and $\alpha\text{-Fe}_2\text{O}_3$ phases, however, the presence of FePO_4 , due to its amorphous nature, has not been verified by X-ray analysis (it should be noted that the transition of amorphous FePO_4 to crystalline phase should take place at ~ 500°C [27]). Sintering at 912 and 930°C with cooling at ~ 0.83 K s⁻¹ leads to the formation of the phosphate layer comprising light grey and dark grey phases, where the dark zone was identified as the

$\text{Fe}_3(\text{PO}_4)_2$ compound and the light grey phase was detected as iron oxides. The presence of $\text{Fe}_3(\text{PO}_4)_2$ is in accord with Kim et al. [28] who postulated that this compound can be created as an intermediate phase at decomposition of FePO_4 into $\text{Fe}_2\text{P}_2\text{O}_7$. X-ray diffraction found the presence of ~ 58 wt-% $\text{Fe}_3(\text{PO}_4)_2$, ~ 16 wt-% FeO , ~ 9 wt-% Fe_2O_3 and ~ 17 wt-% Fe_3O_4 in the phosphate layer. Raman spectroscopy showed intense bands at 940 and 968 cm^{-1} which, in accord with Zhang [29], were attributed to the $\text{Fe}_3(\text{PO}_4)_2$ compound, a less intense band near 1009 cm^{-1} , corresponding to FePO_4 , was also detected. The phase composition of the layer resulting from sintering at 930°C is substantially identical with that after sintering at 912°C. The phosphate layer after sintering at 980°C is composed of a solidified eutectic phase having a lamellar structure consisting of $\text{Fe}_3(\text{PO}_4)_2$ and lamellae of Q phase containing 10% P_2O_5 [30]. The phosphate layer resulting from sintering at 1075°C comprising a lamellar eutectic phase, identified by EDX as $\text{Fe}_3\text{P}_2\text{O}_7$; also the presence of rounded iron oxides up to ~ 20 μm in size were observed. X-ray analysis proved the presence of ~ 45 wt-% $\text{Fe}_3(\text{PO}_4)_2$ and iron oxides with predominance of wüstite at ~ 44 wt-%. In Raman spectrum the bands at 591 and 637 cm^{-1} and at 269-507 cm^{-1} , assigned to wüstite and hematite [31], were found. Sintering at 1130°C and quenching into water (at ~ 150 K s^{-1}) leads to creating a thin continuous layer of solidified eutectic phase with a fine lamellar structure consisting of $\text{Fe}_3(\text{PO}_4)_2$ and long “needles” with sizes up to 10 μm , identified by EDX as $10\text{FeO}\cdot\text{P}_2\text{O}_5$, which corresponds well with the Q phase [30]. Raman spectra from the lamellar matrix exhibited an intense band at ~ 969 cm^{-1} , attributed to ferrous orthophosphate, while Raman spectra from long needles have bands at 396, 602, 680 cm^{-1} well corresponding to wüstite [29]. During sintering at 1130°C and quenching into liquid nitrogen (~ 420 K s^{-1}) the precipitation of the Q phase as long needles was suppressed. The solidified eutectic phase had the same composition as found for lamellar eutectic phase after quenching into water. With much finer lamellae, however, this phase was identified by X-ray analysis as graffonite present in ~ 85 wt-% amount; the iron oxides (magnetite, hematite and wüstite) in ~ 15 wt-% amount were also found. The Raman spectrum showed intense doublet bands near ~ 964 and ~ 1010 cm^{-1} and a wide band between ~ 370 and ~ 680 cm^{-1} , which well agrees with the Raman spectrum of graffonite given in the Database RRUFF™ [32].

The investigation in [26] was aimed towards analyzing the effect of different sintering temperatures and different cooling rates on phosphate layer properties, including some information tests of corrosion resistance of the composites. This communication deals with electrochemical corrosion resistance behaviour of similar sintered composites and further variants are considered, namely 5 wt-% FePO_4 coating, an addition of 1.0 wt-% silica nano-powder and of Fe/ FePO_4 based on irregularly shaped iron particles. These powder mixtures were processed by compaction, sintering and cooling with different rates. Electrochemical corrosion behaviour of sintered composites was investigated and is discussed in relation to microstructural changes in corroded surface areas of the compacts.

2. EXPERIMENTAL

Formulation and preparation conditions of the sintered composites are listed in Table 1. Höganäs AB water atomised ASC100.29 iron powder [33] was the raw material. For the preparation of

phosphate coated powders the irregularly (Figure 1a) and spherically shaped (Figure 1b) iron particles were used.

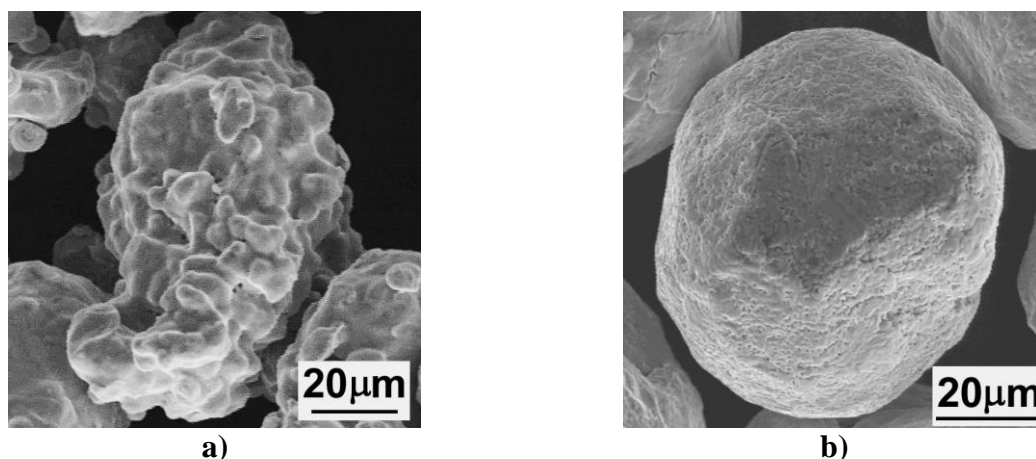


Figure 1. Irregularly (a) and spherically (b) shaped uncoated iron particles

The spherical shape of iron particles was obtained by milling the ASC 100.29 powder in air using a Pallmann mill working at 11000 rpm. The 100-160 μm size fraction of the milled powder was subsequently annealed for 1 hour at 850°C in an atmosphere of N_2 -10 vol-% H_2 . Vickers microhardness of both the irregularly and spherically shaped particles was 110-120 HV0.25. Precipitation coating procedure of the iron powder, described in detail by Brunckova et al. [34], was performed by stirring the iron powder for 120 min at 20°C in a phosphating solution containing acetone and orthophosphoric acid. Using a suitable composition of the phosphating solution (25 ml acetone p.a. + 0.4 ml H_3PO_4 per 25 mg Fe powder and/or 25 ml acetone p.a. + 0.88 ml H_3PO_4 per 25 mg Fe powder) two variants of the coated powders containing 2 and 5 wt-% of the FePO_4 were prepared. The Fe/ FePO_4 coated powders were subsequently dried in air at 60°C for 120 min and then calcined at 400°C in air for 180 min. By adding 1.0 wt-% of silica nano-powder (Fumed Silica, purity of 99.8%, Sigma-Aldrich) the Fe/2 wt-% FePO_4 +1.0 wt-% SiO_2 and Fe/5 wt-% FePO_4 +1.0 wt-% SiO_2 variants were also prepared.

Thus prepared powders were cold pressed in a hard metal die without lubrication into cylindrical compacts (ϕ 10 x 5 mm^3) with a green density ranging from 6650 to 6700 kg m^{-3} . The density was determined by measurement of dimensions with the accuracy of ± 0.01 mm and by weighing with accuracy of ± 0.001 g. Subsequently, the green compacts were sintered in air at temperatures of 912, 930, 980, 1075 and 1130°C, respectively for 3 min in a laboratory tube furnace ANETA 1 with the temperature control $\pm 2^\circ\text{C}$. The heating rate of compacts sintered at 912, 930, 980 and 1075°C was 0.3 K s^{-1} and the cooling rate ~ 0.83 K s^{-1} . In the case of the sintering at 1130°C, the compacts were quenched into cold water with a cooling rate of ~ 150 K s^{-1} and the others into liquid nitrogen at ~ 420 K s^{-1} . To achieve such high cooling rates, the compacts were rapidly transferred from the sintering furnace into a sufficiently large container filled with water or liquid nitrogen with intensive movement of sintered compacts in the cooling medium.

Sintered pure iron powder compacts on the basis of milled Höganäs AB ASC 100.29 iron powder for reference corrosion testing were also prepared.

Table 1. Compacts, formulation and preparation conditions; all samples were compacted to a density of 6650-6700 kg m⁻³ in a hard metal die without lubrication; a size fraction of iron powder was 100-160 μm

Compacts and material		Fe particles	Preparation conditions
<i>A: sintered pure iron</i>			
A1	Fe	Spherical	Sintering at 1120°C/30min/N ₂ +10%H ₂ , cooled at at ~ 0.83 K s ⁻¹
<i>Group B: (Fe/FePO₄)+1wt-% silica nano-powder, sintered and quenched</i>			
B1	Fe/2%FePO ₄ +SiO ₂	Spherical	sintering at 980°C/3min/air with cooling at ~ 0.83 K s ⁻¹ and then sintering at 1130°C in air for 3 min with quenching into liquid nitrogen at ~ 420 K s ⁻¹
B2	Fe/2%FePO ₄ +SiO ₂		sintering at 1130°C/3min/air with quenching into liquid nitrogen at ~ 420 K s ⁻¹
B3	Fe/5%FePO ₄ +SiO ₂		
B5	Fe/5%FePO ₄ +SiO ₂	Irregular	sintering at 980°C in air for 3 min with cooling at ~ 0.83 K s ⁻¹ and then sintering at 1130°C in air for 3 min with quenching into liquid nitrogen at ~ 420 K s ⁻¹
B4	Fe/2%FePO ₄ +SiO ₂		sintering at 1130°C in air for 3min with quenching into liquid nitrogen ~ 420 K s ⁻¹
B6	Fe/5%FePO ₄ +SiO ₂		
<i>Group C: Fe/FePO₄, sintered and cooled at ~ 0.83 K s⁻¹</i>			
C1	Fe/2%FePO ₄	Spherical	sintering at 912°C in air for 3min with cooling at ~ 0.83 K s ⁻¹
C2	Fe/2%FePO ₄		sintering at 930°C in air for 3 min with cooling at ~ 0.83 K s ⁻¹
C3	Fe/2%FePO ₄		sintering at 980°C in air for 3 min with cooling at ~ 0.83 K s ⁻¹
C4	Fe/2%FePO ₄		sintering at 1075°C in air for 3 min with cooling at ~ 0.83 K s ⁻¹
<i>Group D: Fe/FePO₄, sintered and quenched</i>			
D1	Fe/5%FePO ₄	Spherical	sintering at 1130°C in air for 3 min with quenching into water at ~ 150 K s ⁻¹
D2	Fe/5%FePO ₄		sintering at 1130°C in air for 3 min with quenching into liquid nitrogen at ~ 420 K s ⁻¹

Electrochemical corrosion testing was performed in similar conditions as reported in our earlier work [26]: The potentiodynamic polarization testing was conducted in 1 mol l⁻¹ NaCl solution with pH 5.6 prepared by using doubly distilled water. Before measurements, the electrolyte was de-aerated with gaseous N₂ for 10 min. Electrochemical measurements were performed using a computer-controlled Autolab PGSTAT 302N potentiostat with three-electrode cell consisting of the specimen (as a working electrode), the reference electrode of Ag/AgCl/KCl (3 mol/l) and Pt plate working as a counter electrode. The potential was scanned at a rate 0.1 mV/s in the range from - 800 mV to + 300 mV. To obtain the corrosion potential and corrosion rate, the Tafel extrapolation method was used. Before

corrosion testing, the specimen surface layer affected by the quenching medium, thickness of 200-250 μm , was removed by dry sanding with fine sandpaper (Struers, Silicon Carbide Paper, FEPA#2400).

Microstructure of composites and their changes in corroded areas were studied by light microscopy (Olympus GX71) and scanning electron microscopy using Jeol-JSM-7000F instrument equipped with EDX spectroscopy microanalyser INCA.

Electrochemical corrosion testing was performed in similar conditions as reported in our earlier work [26]: The potentiodynamic polarization testing was conducted in 1 mol l^{-1} NaCl solution with pH 5.6 prepared by using doubly distilled water. Before measurements, the electrolyte was de-aerated with gaseous N_2 for 10 min. Electrochemical measurements were performed using a computer-controlled Autolab PGSTAT 302N potentiostat with three-electrode cell consisting of the specimen (as a working electrode), the reference electrode of Ag/AgCl/KCl (3 mol/l) and Pt plate working as a counter electrode. The potential was scanned at a rate 0.1 mV/s in the range from - 800 mV to + 300 mV. To obtain the corrosion potential and corrosion rate, the Tafel extrapolation method was used. Before corrosion testing, the specimen surface layer affected by the quenching medium, thickness of 200-250 μm , was removed by dry sanding with fine sandpaper (Struers, Silicon Carbide Paper, FEPA#2400).

Microstructure of composites and their changes in corroded areas were studied by light microscopy (Olympus GX71) and scanning electron microscopy using Jeol-JSM-7000F instrument equipped with EDX spectroscopy microanalyser INCA. Raman spectroscopy was performed using HORIBA Scientific XploRA system spectrometer with a He-Ne laser (532 nm).

3. RESULTS AND DISCUSSION

3.1 Microstructure of sintered composites

In Figures 2a-c and Figures 3a, b the micrographs of the microstructure of sintered composites based on phosphate coated spherically shaped iron powder with 5 wt% FePO_4 are presented. The original iron particles are surrounded with a phosphate layer having a phase composition resulting from applied processing conditions. The formation of the eutectic phase during sintering at 1130°C and its fast solidification by quenching into water or into liquid nitrogen (Figures 3a, b) leads to the creation of a thin and continuous phosphate layer having a fine lamellar structure. It should be noted that microscopic observations of the phosphate layer formed during the sintering in the temperature range 912 to 1075°C with cooling at $\sim 0.83 \text{ K s}^{-1}$ revealed the presence of some discontinuities, probably associated with heterogeneous phase composition of the layer. Raman spectrum in Figure 4, scanned from a fine lamellar phosphate layer, shows intense doublet bands 964 and $\sim 1010 \text{ cm}^{-1}$ and a wide band between ~ 370 and 680 cm^{-1} . This is in good agreement with Raman spectrum presented in [26], as well as with Raman spectrum of graffonite according to Database in Ref. [32].

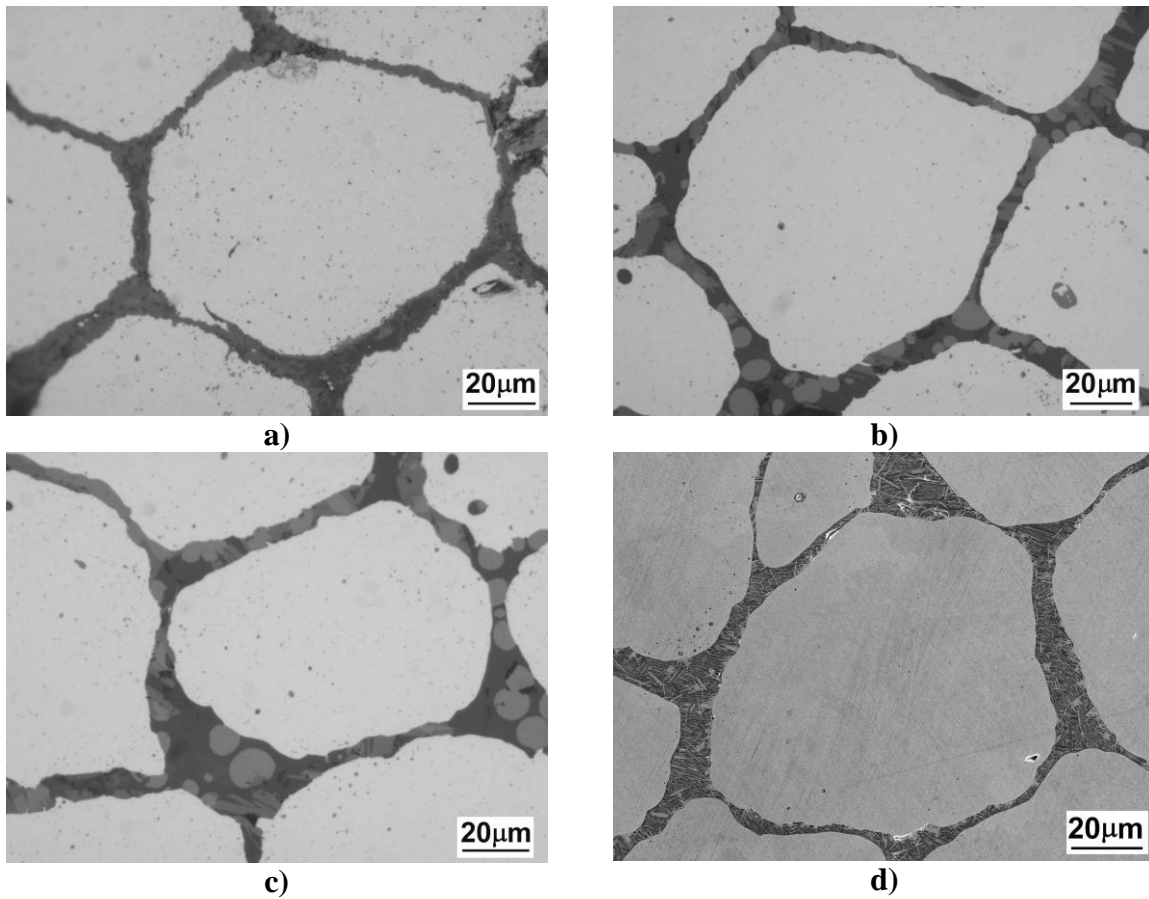


Figure 2. Microstructure of the composites with the phosphate layer resulting from sintering at 912°C (a), at 980°C (b), at 1075°C (c) and cooled at 0.83 K s⁻¹; the micrograph (d) shows the microstructure after sintering at 1130°C with quenching into water at ~150 K s⁻¹

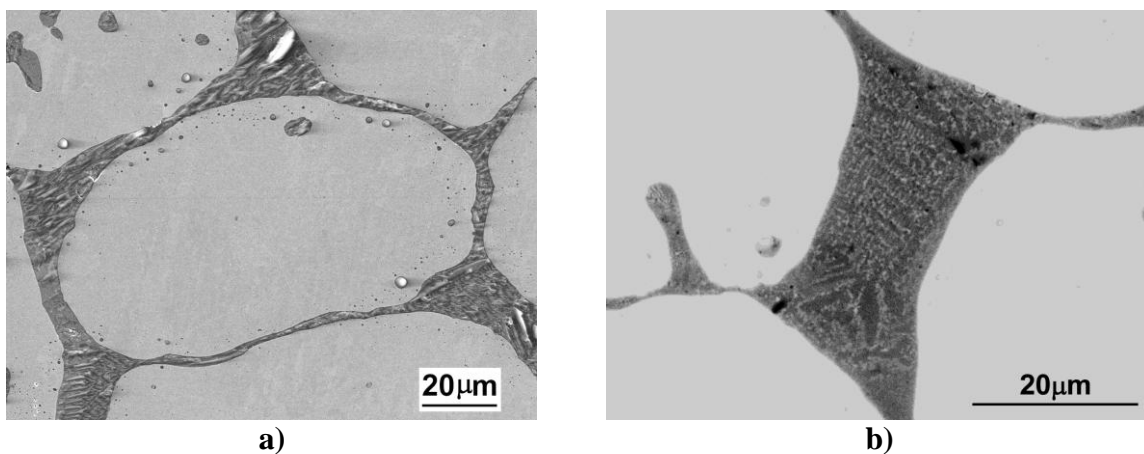


Figure 3. Microstructure of the composites with the phosphate layer resulting from sintering at 1130°C with quenching into liquid nitrogen at ~ 420 K s⁻¹ (a), the phosphate layer in detail (b)

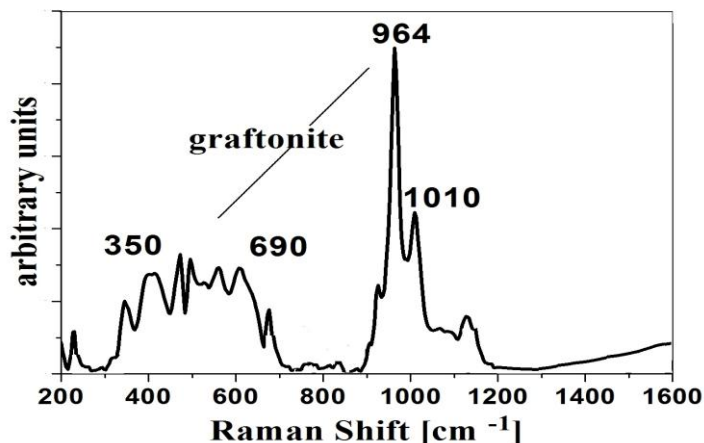


Figure 4. Raman spectrum scanned from a fine lamellar structure of the phosphate layer in a composite sintered at 1130°C and quenched into liquid nitrogen

It was expected that the addition of silica nano-powder, variations of $\text{Fe}/\text{FePO}_4+\text{SiO}_2$, along with a positive action of liquid phase created during sintering at 1130°C, would improve the protective effect of phosphate coatings against corrosion. However, the microscopic observations have shown that the silica nano-powder particles tend to agglomerate and so they can deteriorate a continuity of the phosphate layer, as shown in the example in Figure 5.

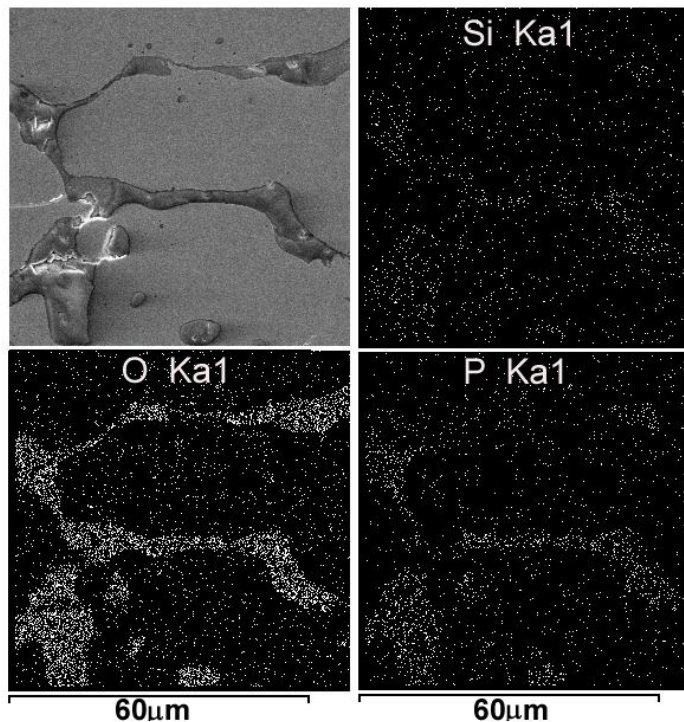


Figure 5. The microstructure and EDX maps of silicon, oxygen and phosphorus distribution in composite designated B6 ($\text{Fe}/5\text{wt}\% \text{FePO}_4+1 \text{ wt}\% \text{ silica nano-powder}$); note that the silica nano-powder particles tend to agglomerate and thus deteriorate the continuity of the phosphate layer

3.2 Electrochemical corrosion behaviour

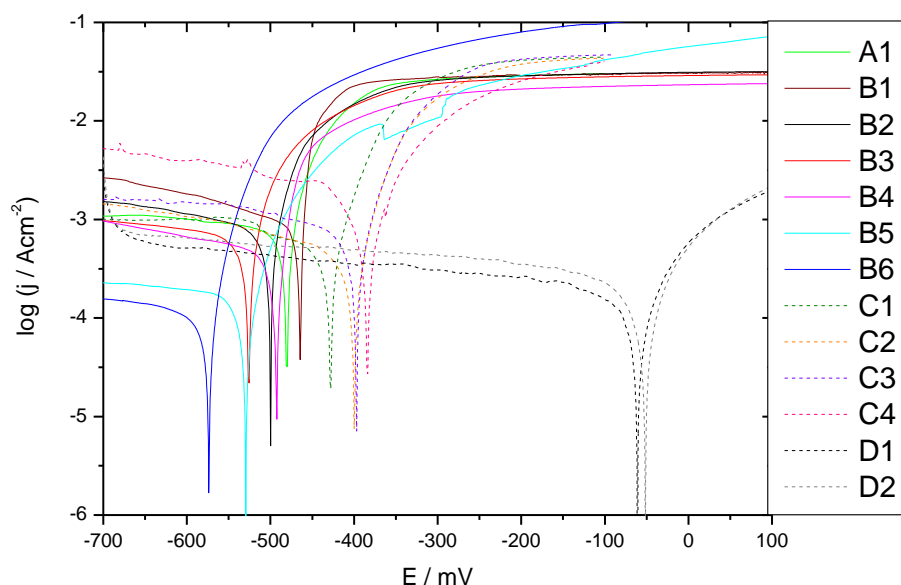


Figure 6. Potentiodynamic polarization curves of sintered composites B1-B6, C1-C4, D1, D2 and of reference pure iron compacts A1 in 1 mol l⁻¹ NaCl solution

Table 2 The values of E_{corr} , j_{corr} and rate of corrosion in a 1 mol l⁻¹ NaCl solution obtained from the potentiodynamic polarization curves of sintered composites B1-B6, C1-C4, D1, D2 and of pure iron compacts A1

Samples	E_{corr} mV	j_{corr} $\mu\text{A}/\text{cm}^2$	Rate of corrosion mm/year
A: sintered pure iron			
A1	-477.3	11453.0	17.2
Group B: (Fe/FePO ₄)+1.0 wt.% SiO ₂ nano-powder, sintered and quenched			
B1	-468.7	1152.7	13.4
B2	-503.0	1002.0	12.1
B3	-524.9	922.7	10.7
B4	-492.7	574.1	6.7
B5	-529.5	461.7	5.4
B6	-573.7	213.1	2.5
Group C: (Fe/FePO ₄), sintered, cooled at ~50°C/min			
C1	-422.9	1.91	2.9
C2	-400.3	1.71	2.6
C3	-397.5	1.62	2.4
C4	-385.8	1.57	2.4
Group D: (Fe/FePO ₄), sintered and quenched			
D1	-51.4	1.41	2.1
D2	-61.8	1.42	2.1

In Figure 6 the polarization curves in 1 mol l^{-1} NaCl solution are presented. The values of E_{corr} (corrosion potential), j_{corr} (corrosion current density) and corrosion rate for sintered composites, B1-B6, C1-C4, D1, D2 (see Table 1) and for reference pure iron compacts A1 are listed in Table 2. The rate of corrosion was calculated from the intersection of the anodic and cathodic Tafel lines' extrapolation.

The highest rate of corrosion was exhibited by pure iron compacts (A1). In view of the rate of corrosion calculated from corrosion current densities, the composites can be classified into three groups relating to processing conditions. To understand the difference in corrosion behavior of individual groups of composites microscopic analysis of the microstructure of the compacts in surface areas affected by corrosion was performed.

3.3 Microscopic analysis of samples after corrosion resistance testing

The microstructure of sintered pure iron is composed of polyhedral grains of α -Fe (ferrite) and porosity of $\sim 8.0\%$, which consists predominantly of irregularly shaped pores distributed along previous iron particle surfaces. Due to the dissolution of the surface of pure iron by acting aggressive chloride ions, a layer of corrosion products, having a black colour, is created, Figure 7a. It can be seen that the corrosion products were created not only on the surface of the composite compacts, but also on free surfaces of open pores communicating with the surface of the compact. The corrosion processes were extended into the corroded compact to a depth of more than $250 \mu\text{m}$. EDS analysis of the surface corrosion products found the composition of $33 \pm 1 \text{ at-\% Fe}$ and $53 \pm 1.5 \text{ at-\% O}$, which corresponds well to the Fe_3O_4 oxide; the amount of $3.3 \pm 0.4 \text{ at-\% Cl}$ was also measured.

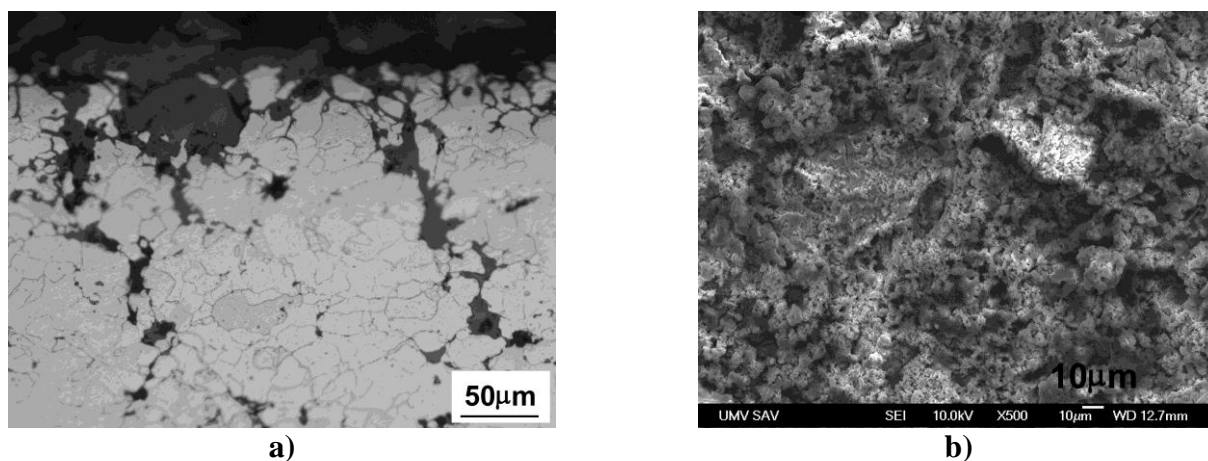


Figure 7. a) Microstructure of the pure iron compact (A1) observed on the cross-section perpendicular to the corroded surface, b) morphology of the surface of corrosion layer; the colour of the corrosion products is black.

From the data in Table 2 it is seen that a protective layer based on the phosphate coating reduces the rate of corrosion by nearly an order of magnitude, when compared with sintered pure iron.

For composites C1-C4 prepared by sintering at 912, 930, 980 and 1075°C, with cooling at $\sim 0.83 \text{ K s}^{-1}$, the corrosion rate of 2.4-2.9 mm year⁻¹ was detected. It appears that increase in the sintering temperature slightly decreases the corrosion rate which can be explained by positive effect of eutectic phase, created at a temperature equal to or higher than 980°C, on improved continuity of the protective phosphate layer. With increasing sintering temperature from 912 to 1075°C, the corrosion potential becomes more positive, while the current density and the rate of corrosion of composites sintered at higher temperature slightly decreases, but the differences in densities of corrosion current between the composites in this group C are not significant.

A relatively significant decrease in the rate of corrosion for composites D1 and D2 sintered at 1130°C and quenched into water and/or into liquid nitrogen, especially when compared to the value for pure iron, is linked with a shift of both cathodic and anodic branches of the polarization curves towards lower current densities with a positive shift in corrosion potential E_{corr} . It is obvious that a thin and continuous layer of the solidified eutectic phase forms an effective barrier to the development of corrosion processes. In Figure 8a the surface of the corrosion layer is shown; this is not completely continuous and the “network” of phosphate layer can be seen. Figure 8b shows that the corrosion processes progressed only through iron particles that were not protected with the solidified eutectic phase, because it was partly removed by slightly sanding the surface of the sintered compact. It is seen that corrosion has spread only to a depth corresponding to the size of the particles.

In the case of composites with 1.0 wt-% silica nano powder, composites B1-B6, processed by sintering at 1130°C and quenched into liquid nitrogen, the expected improvement in corrosion resistance was not achieved. It was found that the corrosion rate, ranging from 13 to 2.5 mm year⁻¹, is influenced by the shape of the iron particles and depends also upon the amount of the FePO₄ coating. The lower rate of corrosion is reached for irregularly shaped iron particles and higher content of the iron phosphate coating.

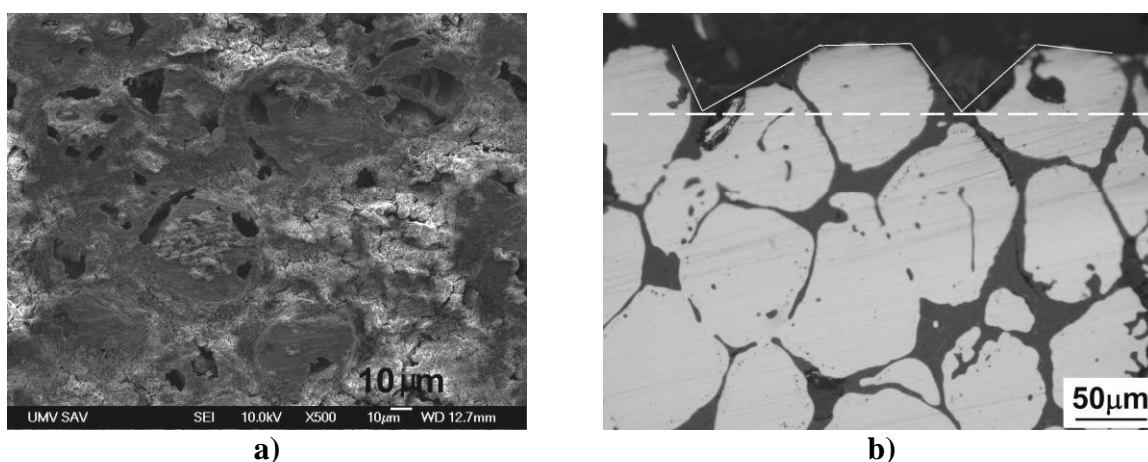


Figure 8. Corrosion of the sample sintered at 1130°C and quenched into liquid nitrogen (sample D2): the surface layer of corrosion products (a), the depth extension of the corrosion processes (b).

It should be noted that the reduced rate of corrosion rate is linked to a shift of both cathodic and anodic branches of the polarization curves towards lower current densities with a slightly negative shift

in corrosion potential (E_{corr}) when compared to values for pure iron compacts. Figure 9a shows the extension of corrosion processes to a depth greater than the size of the iron particles. Such corrosion behaviour of the composites belonging to the group B may be due to discontinuities of iron phosphate layer caused by agglomeration of silica nano-powder particles. In Figure 9b the network of iron phosphate insulating layer after the corrosion test is shown; this confirms the corrosion resistance of applied coating comprising a solidified eutectic phase.

In the case of composites with 1.0 wt-% silica nano powder, composites B1-B6, processed by sintering at 1130°C and quenched into liquid nitrogen, the expected improvement in corrosion resistance was not achieved. It was found that the corrosion rate, ranging from 13 to 2.5 mm year⁻¹, is influenced by the shape of the iron particles and depends also upon the amount of the FePO₄ coating. The lower rate of corrosion is reached for irregularly shaped iron particles and higher content of the iron phosphate coating. It should be noted that the reduced rate of corrosion rate is linked to a shift of both cathodic and anodic branches of the polarization curves towards lower current densities with a slightly negative shift in corrosion potential (E_{corr}) when compared to values for pure iron compacts. Figure 9a shows the extension of corrosion processes to a depth greater than the size of the iron particles. Such corrosion behaviour of the composites belonging to the group B may be due to discontinuities of iron phosphate layer caused by agglomeration of silica nano-powder particles.

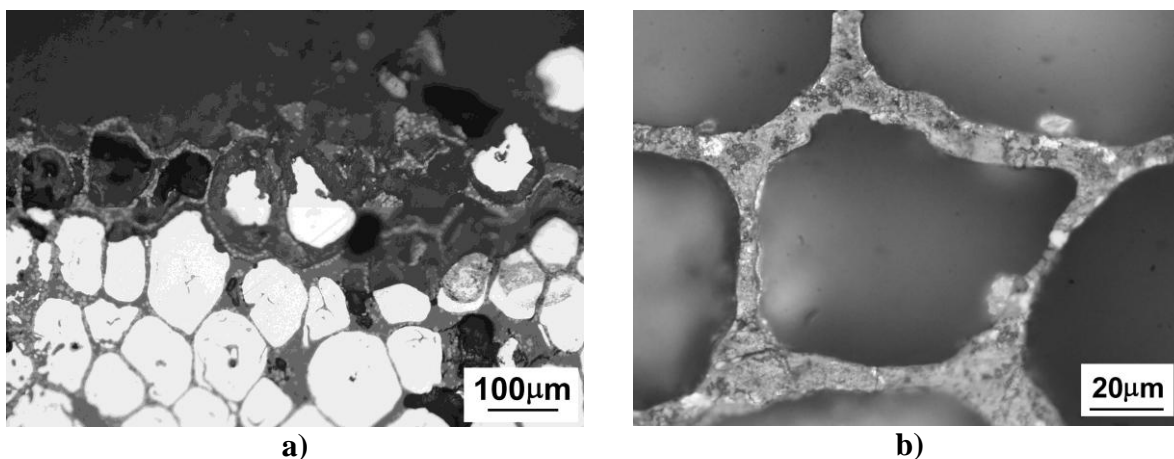


Figure 9. The extension of corrosion processes in composite B3 (Fe/FePO₄+1.0 wt-% silica nano-powder) sintered at 1130°C and quenched into liquid nitrogen (a), the network of iron phosphate insulating layer after corrosion - section through the corroded layer (b).

In Figure 9b the network of iron phosphate insulating layer after the corrosion test is shown; this confirms the corrosion resistance of applied coating comprising a solidified eutectic phase.

4. CONCLUSIONS

Sintered composites with a network of a thin phosphate layer surrounding α -iron areas were prepared on the basis of iron powder coated with 2 and 5 wt-% ferric phosphate FePO₄. The coated

powders were processed by cold pressing and sintering at temperatures ranging from 912 to 1130°C in air for 3 min. Sintering at 1130°C, with sufficiently high cooling rate by quenching into water or into liquid nitrogen, results in the creation of a thin and continuous protective layer of solidified eutectic phase covering the original iron particles. This layer consists of ~ 85 wt-% of a fine lamellar structure identified as graffonite $\text{Fe}_3(\text{PO}_4)_2$ with needles of wüstite. When quenching into liquid nitrogen, a high cooling rate, the growth of the needles of wüstite is suppressed.

Electrochemical corrosion behaviour was investigated using potentiodynamic polarization tests. A significant improvement in corrosion resistance was detected in the case of sintering at 1130°C and quenching into water ($\sim 150 \text{ K s}^{-1}$), or quenching into liquid nitrogen with a cooling rate of $\sim 420 \text{ K s}^{-1}$. The corrosion potential was positively shifted to about -50 or -60 mV, indicating more passive conditions. However, a moderate reduction in the corrosion current density, as well as the reduction of the rate of corrosion, was observed.

The phosphate protective layer reduces the rate of corrosion by nearly an order of magnitude, when compared to sintered pure iron. For composites prepared by sintering at temperatures ranging from 912 to 1075°C and by cooling at $\sim 0.83 \text{ K s}^{-1}$, the corrosion rate ranged from 2.4 to 2.9 mm year⁻¹. Increasing the sintering temperature slightly decreases the corrosion rate, the corrosion potential becomes more positive, but the differences in densities of corrosion current are not significant.

In the case of composites with an addition of 1.0 wt-% silica nano powder, sintered at 1130°C and quenched into liquid nitrogen at $\sim 420 \text{ K s}^{-1}$, the expected improvement in electrochemical corrosion resistance was not achieved. This was explained by the formation of some discontinuities in protective phosphate layer due to the agglomeration of silica nano-powder.

The investigation of electrochemical corrosion behaviour and its correlation with microstructural observations of corroded surfaces of composites prepared on the basis of a coated Fe/FePO₄ powders showed that a thin and continuous layer of the solidified eutectic phase may act as an effective barrier to the extension of corrosion processes.

ACNOWLEDGEMENT

The authors wish to thanks to the Slovak National Grant Agency (Projects VEGA 2/0052/14, 2/0100/15, 1/0211/12) and Slovak Research and Development Agency through project APVV-0222-10 for financially supporting this work.

References

1. C. A. Borrás, R. Romagnoli and R. Lezna, *Electrochimica Acta*, 45 (2000) 1717.
2. S. Ponmariappan, S. Maruthamuthu, N. Palaniswamy and R. Palaniappan, *Corrosion Reviews*, 22 (2004) 307.
3. Y. Gonzalez, M. Lafont, N. Pebere, G. Chatainier, J. Roy and T. Bouissou, *Corrosion Science*, 37 (1995) 1823.
4. A. Bittner, H. Heubach, *Journal of Coatings Technology*, 61 (1989) 111.
5. S. Rebeyrat, J. L. Grosseau-Poussard, J. F. Dinhut and P. O. Renault, *Thin Solid Films*, 379 (2000) 139.

6. F. Zhang, The Mussel Adhesive Protein (Mefp-1) — A GREEN Corrosion Inhibitor, Doctoral Thesis, KTH Chemical and Science and Engineering, Stockholm, Sweden 2013-12-08, <http://www.divaportal.org/smash/get/diva2:626667/FULLTEXT01.pdf>.
7. H. P. Volkland, H. Harms, B. Müller, G. Repphun, O. Wanner and A. J. B. Zehnder, *Applied and Environmental Biology*, 66 (2000) 4389.
8. K. Zaghbi and C. M. Julien, *J. Power Sources*, 142 (2005) 279.
9. Y. Xu, Y. Lu, P. Yin, L. Yan, Z. Yang, R. Yang, *Journal of Materials Processing Technology*, 204 (2008) 513.
10. N. Aliouane, T. Badeche, Y. Gagou, E. Nigrelli and P. Saint-Gregoire, *Ferroelectrics*, 241 (2000) 255.
11. Y.-S. Hong, Y. J. Park, K. S. Ryu and S. H. Chang, *Solid State Ionics*, 156 (2003) 1-2, 27.
12. Y. Song, P. Y. Zavalij, M. Suzuki and M. S. Whittingham, *Inorg. Chem.* 41 (2002) 5778.
13. C. R. Rambo, L. Ghussn, F. F. Sene, J. R. Martinelli, *Journal of Non-Crystalline Solids*, 352 (2006) 3739.
14. Y. Makhkhas, S. Aqdim, El H. Sayouty, *Journal of Materials Science and Chemical Engineering*, 1 (2013) 3, 1. Article ID:35297, DOI:10.4236/msce.2013.13001.
15. B. C. Sales, L. A. Boatner, *J. Am. Ceram. Soc.* 70 (1987) 615.
16. D. E. Day, Z. Wu, C. S. Ray, P. R. Hrma, *J. Non-Cryst. Solids*, 241 (1998) 1.
17. R. K. Brow, *Journal of Non-Crystalline Solids*, 263/264 (2000) 1.
18. J. Fu, *J. Mater. Sci.*, 33 (6) (1998) 1549.
19. J. B. Bates, N. J. Dudney, G. R. Gruzalski, R. A. Zuhr, A. Choudhury, C. F. Luck, J. D. Robertson, J. B. Bates, N. J. Dudney, G. R. Gruzalski, R. A. Zuhr, A. Choudhury, C. F. Luck and J. D. Robertson, *Solid State Ionics*, 53-56 (1992), 647.
20. S. Ray, X. Fang, M. Karabulut, G. K. Marasinghe and D. E. Day, *Journal of Non-Crystalline Solids*, 249 (1999) 1, 1. doi:10.1016/S0022-3093(99)00304-X
21. H. Niida, M. Takahashi, T. Uchino and T. Yoko, *Journal of Non-Crystalline Solids*, 306 (2002) 292. doi:10.1016/S0022-3093(02)01188-2.
22. I. W. Donald, *Glass Technol.*, 48 (2007), 155.
23. M. I. Ojovan, W.E. Lee, *Metallurgical and Materials Transactions A*, 42 (2011) 837.
24. C.-W. Kim and D. E. Day, *J. Non-Cryst. Solids*, 331 (2003) 20.
25. I. Wacawska and M. Szumera, *J. Therm. Anal. Calorim.*, 101 (2010) 423.
26. E. Dudrova, M. Kabatova, P. Hvizdos and R. Orinakova, *Surf. Interface Analysis*, 47 (2015) 350.
27. Y. Xiao, W. Pu, W. Wan, Y. Cui, *Int. J. Electrochem. Sci.*, 8 (2013) 938.
28. J. Kim, K.-Y. Park, I. Park, J.-K. Yoo, J. Hong and K. Kang, *J. Mater. Chem.*, 22 (2012) 1964.
29. L. Zhang, Phase equilibria in iron phosphate system. A Dissertation, Missouri University of Science and Technology, 2010.
http://scholarsmine.mst.edu/thesis/Phase_equilibria_in_007dcc80907f7d
30. G. Trömel and K. Schwerdtfeger, *Arch. Eisenhüttenwesen*, 34 (1963) 55.
31. M. Hanesch, *Geophys. J. Int.*, 177 (2009) 941.
32. Graftonite - RRUFF Database: Raman, X-ray, Infrared, <http://rruff.info/Graftonite>
33. Höganäs Handbook for Sintered Components, Material and Powder Properties, 1, Höganäs AB (1997).
34. H. Brunckova, M. Kabatova, E. Dudrova, *Surf. Interface Analysis*, 42 (2010) 13.